



OPEN

Machine learning-driven electronic identifications of single pathogenic bacteria

Shota Hattori¹, Rintaro Sekido¹, Iat Wai Leong², Makusu Tsutsui²✉, Akihide Arima³, Masayoshi Tanaka¹, Kazumichi Yokota⁴, Takashi Washio², Tomoji Kawai²✉ & Mina Okochi¹✉

A rapid method for screening pathogens can revolutionize health care by enabling infection control through medication before symptom. Here we report on label-free single-cell identifications of clinically-important pathogenic bacteria by using a polymer-integrated low thickness-to-diameter aspect ratio pore and machine learning-driven resistive pulse analyses. A high-spatiotemporal resolution of this electrical sensor enabled to observe galvanotactic response intrinsic to the microbes during their translocation. We demonstrated discrimination of the cellular motility via signal pattern classifications in a high-dimensional feature space. As the detection-to-decision can be completed within milliseconds, the present technique may be used for real-time screening of pathogenic bacteria for environmental and medical applications.

Bacteria constitute a major class of pathogens in environments including water and food^{1–3}. They are evolved in distinct ways to spontaneously move by using motile filamentous organelle protruding from the micrometer-scale bodies for invading in organisms and multiply themselves. While many of them are innocuous, there are also toxic strains that may bring detrimental impacts on health of individuals to global economy through causing infection disease outbreaks. Plate counting and polymerase chain reaction-based genomic analyses have thus been used as effective means to inspect presence or absence of bacteria in biosamples. However, the methods in general involve many pretreatment steps and thus time-consuming often requiring hours for the tests to be completed^{4,5}, despite that the risk of infection outspread rises quickly in general as the microbes grow in number in the hosts. It is therefore of urgent importance to construct a reliable and highly-sensitive sensor for rapid analyses of viable microbes at an early stage of infection.

Here we report on use of solid-state micropores for label-free single-cell discriminations of five clinically-important pathogenic bacteria, *Staphylococcus aureus*, *Pseudomonas fluorescens*, *Salmonella enterica*, *Escherichia coli* and *Bacillus cereus*^{6–9}, by their unique motility. The working mechanism is based on single-cell detections via Coulter principle that measures transient drops in the cross-membrane ionic current upon translocation of microbes through the conduit¹⁰. Unlike the conventional Coulter counters having relatively high thickness-to-diameter aspect ratio channel structures, a special care was taken in the present study to exploit it for detecting bacterial motility by employing a low aspect ratio pore architecture^{11–13} to make the ionic current more sensitive to multiple physical parameters of analytes such as shape^{14,15}, surface charge density¹⁶, mass^{17,18}, surface proteins^{19,20}, and even the translocation motions²¹. Furthermore, since the enhanced sensor sensitivity is expected to yield more complicated ionic current signal patterns, we employed machine learning to pattern-analyze bacteria-derived fine features in the electrical signatures so as to compare and discern the multitude of physical properties of individual microbes in a high dimensional feature space.

¹Department of Chemical Science and Engineering, School of Materials and Chemical Technology, Tokyo Institute of Technology, 2-12-1, O-okayama, Meguro-ku, Tokyo 152-8552, Japan. ²The Institute of Scientific and Industrial Research, Osaka University, Mihogaoka 8-1, Ibaraki, Osaka 567-0047, Japan. ³Department of Biomolecular Engineering, Graduate School of Engineering, Nagoya University, Furo-cho, Chikusa-ku, Nagoya 464-8603, Japan. ⁴National Institute of Advanced Industrial Science and Technology, Takamatsu, Kagawa 761-0395, Japan. ✉email: tsutsui@sanken.osaka-u.ac.jp; kawai@sanken.osaka-u.ac.jp; okochi@chemeng.titech.ac.jp

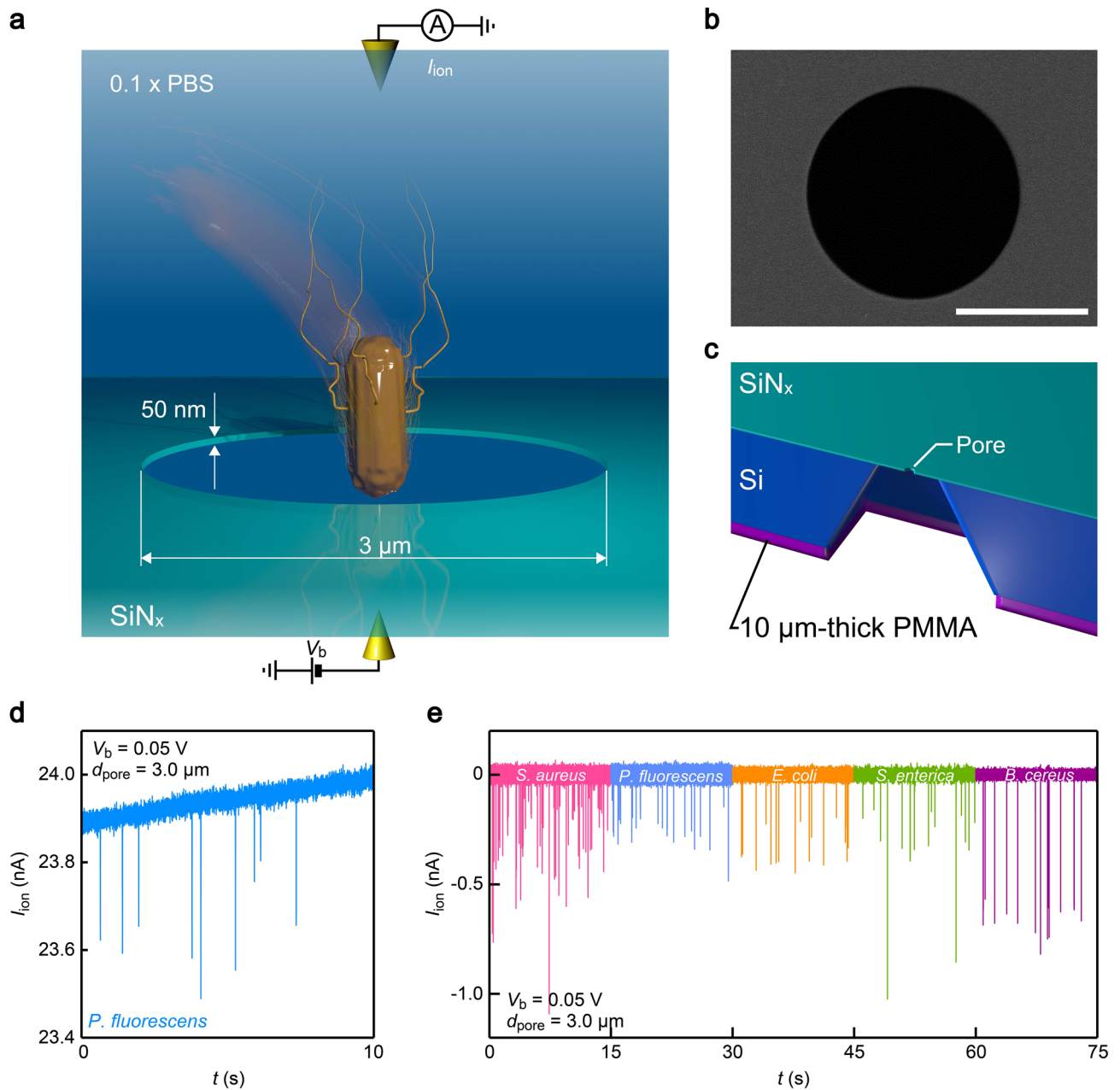


Figure 1. Single-bacteria detections using a low thickness-to-diameter aspect ratio micropore. **(a)** A sketch depicting a bacterium captured into a 3 μm-sized pore sculpted in a 50 nm-thick SiN_x membrane. The associated transient change in the ionic current I_{ion} through the pore was measured using a pair of Ag/AgCl electrodes under the applied voltage V_b . **(b)** A scanning electron micrograph of a micropore. Scale bar denotes 2 μm. **(c)** A model depicting the cross-sectional view of the pore chip. On the backside of the substrate, 10 μm-thick polymethyl methacrylate (PMMA) layer was coated for reducing the device capacitance. **(d)** I_{ion} versus time (t) trace recorded in 0.1 × PBS containing *P. fluorescens* with a micropore of diameter $d_{pore} = 3.0$ μm under $V_b = 0.05$ V. **(e)** Resistive pulses observed in dispersion solution of the five pathogenic bacteria. Color coding is: pink = *S. aureus*, cyan = *P. fluorescens*, orange = *E. coli*, green = *S. enterica*, and purple = *B. cereus*. Open pore current is offset to zero.

Results

The micropore consists of a lithographically-defined hole of diameter d_{pore} formed in a 50 nm thick SiN_x membrane (Fig. 1a,b). In experiments, bacteria dispersed in phosphate buffer saline (PBS) was added to one side of the membrane while the other side was filled with only PBS. Two Ag/AgCl rods were then used as electrodes to measure the ionic current I_{ion} flowing through the microscale conduit under the applied dc voltage V_b . Backside of the substrate was coated with a micrometer-thick PMMA layer (Fig. 1c) to reduce the device capacitance for

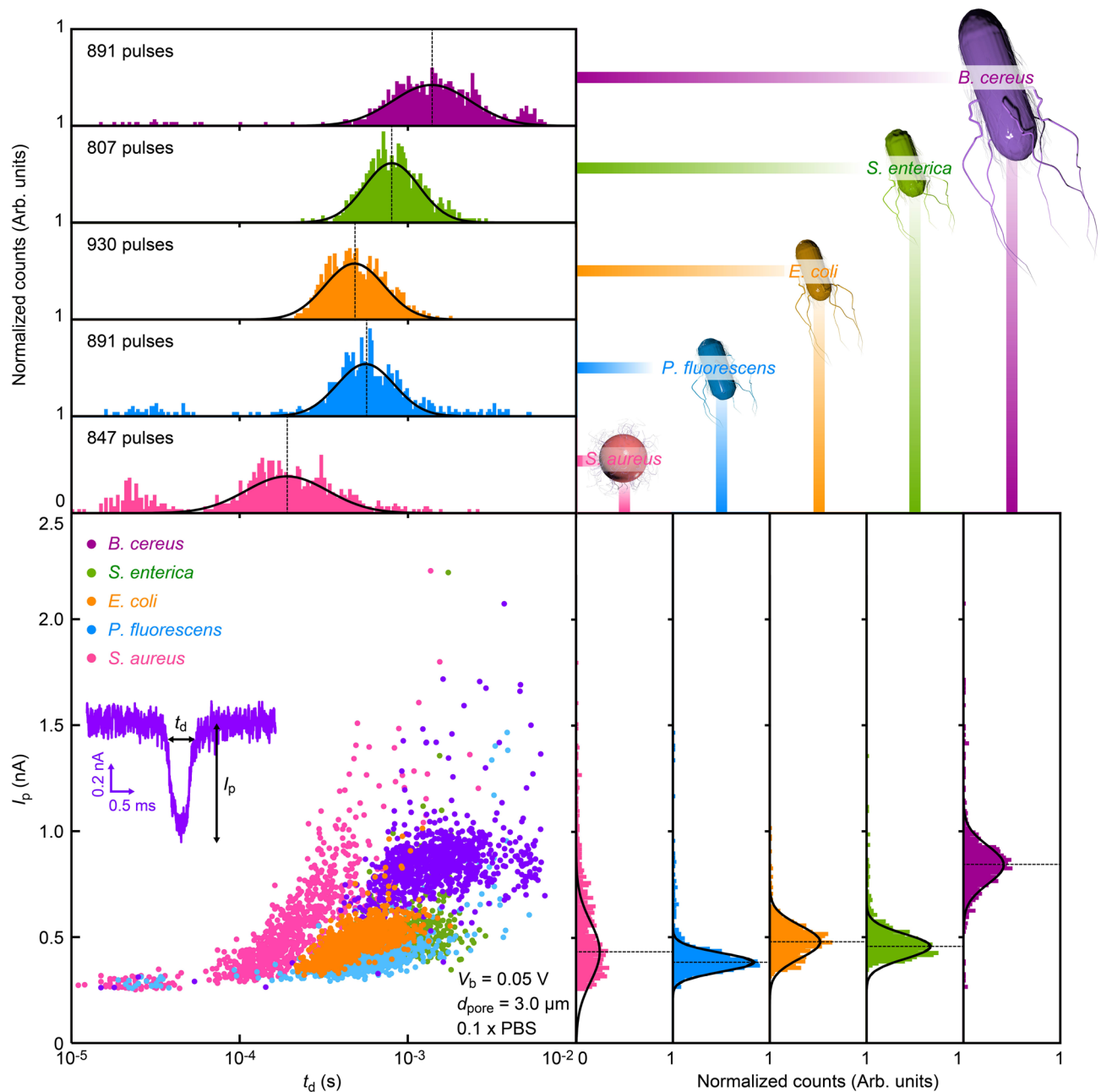


Figure 2. Resistive pulse patterns of pathogenic bacteria. The pulse height I_p versus width t_d scatter plots (bottom left) and corresponding histograms. The counts are normalized by the number of resistive pulses. Color code denotes: pink = *S. aureus*, cyan = *P. fluorescens*, orange = *E. coli*, green = *S. enterica*, and purple = *B. cereus* as also described schematically in the top right. Dotted lines point the center of I_p and t_d distributions defined by Gaussian fits.

lowering high-frequency current noise²² as well as to ensure fast temporal resolution of the sensor²³ for detecting rapid change in I_{ion} during the single-cell translocation.

The ionic current through the SiN_x pore of diameter $d_{pore} = 3 \mu\text{m}$ was measured to be around 24 nA at $V_b = 0.05 \text{ V}$ (Fig. 1d). This manifests the predominant influence of the access resistance²⁴ $R_{acc} = \rho/d_{pore} = 2 \text{ M}\Omega$ on I_{ion} compared to the component $R_{pore} = 4\rho L/\pi d_{pore}^2 = 42 \text{ k}\Omega$ inside the channel, where $L = 50 \text{ nm}$ is the channel depth and $\rho = 6 \Omega\text{m}$ is the resistivity of the electrolyte buffer. Meanwhile, each time when a bacterium passed through the pore, it temporarily blocked the ion flow thereby caused a pulse-like I_{ion} drop (Fig. 1e).

The I_{ion} signatures are anticipated to reflect the intrinsic physical properties of the bacteria. To see if there is any difference in the resistive pulse profiles among the five species, therefore, we constructed scatter plots of the signal height I_p as a function of the width t_d that are known to represent the characteristic size and the time required for the cell to pass through the micropore, respectively (Fig. 2). As a result, we found significant overlap

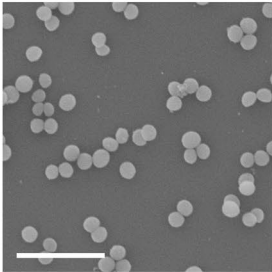
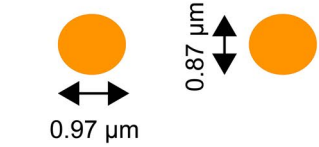
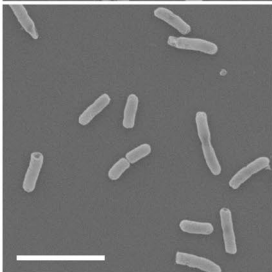
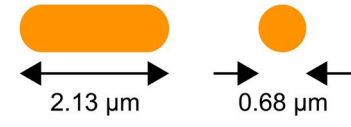
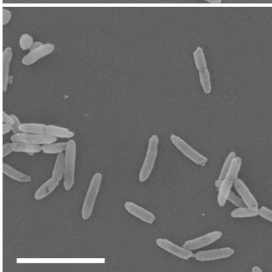
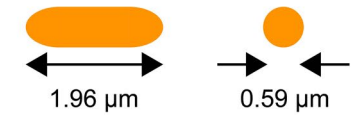
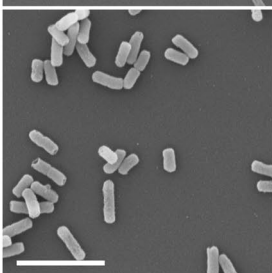
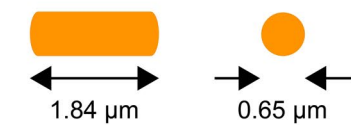
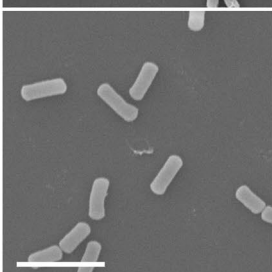
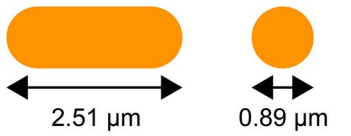
Bacteria	Scanning electron microscopy images	Characteristic size/shape (Length) (Diameter)
<i>S. aureus</i>		 0.97 μm 0.87 μm
<i>S. enterica</i>		 2.13 μm 0.68 μm
<i>P. fluorescens</i>		 1.96 μm 0.59 μm
<i>E. coli</i>		 1.84 μm 0.65 μm
<i>B. cereus</i>		 2.51 μm 0.89 μm

Table 1. Size and shape of pathogenic bacteria. Scale bars denote 5 μm .

in their distributions, naturally interpreted as a consequence of their resembling micrometer-scale morphologies as confirmed by electron microscope observations (Table 1).

Under this circumstance, it becomes important to explore other features in the I_{ion} signatures that can better distinguish the pathogenic bacteria. For this, we first investigated the physical origins of the variations in the resistive pulse patterns by performing finite element simulations¹³ of the cross-membrane ionic current. We built three-dimensional models of the bacteria deduced from their morphologies depicted in the scanning electron micrographs. By changing the position z of the modeled structure along the axial direction, we obtained I_{ion} blockade characteristics for the five microbes (Fig. 3a), where we tentatively assumed an up-right orientation of the cell with respect to the membrane surface. The theoretical resistive pulses were then compared to the I_{ion}

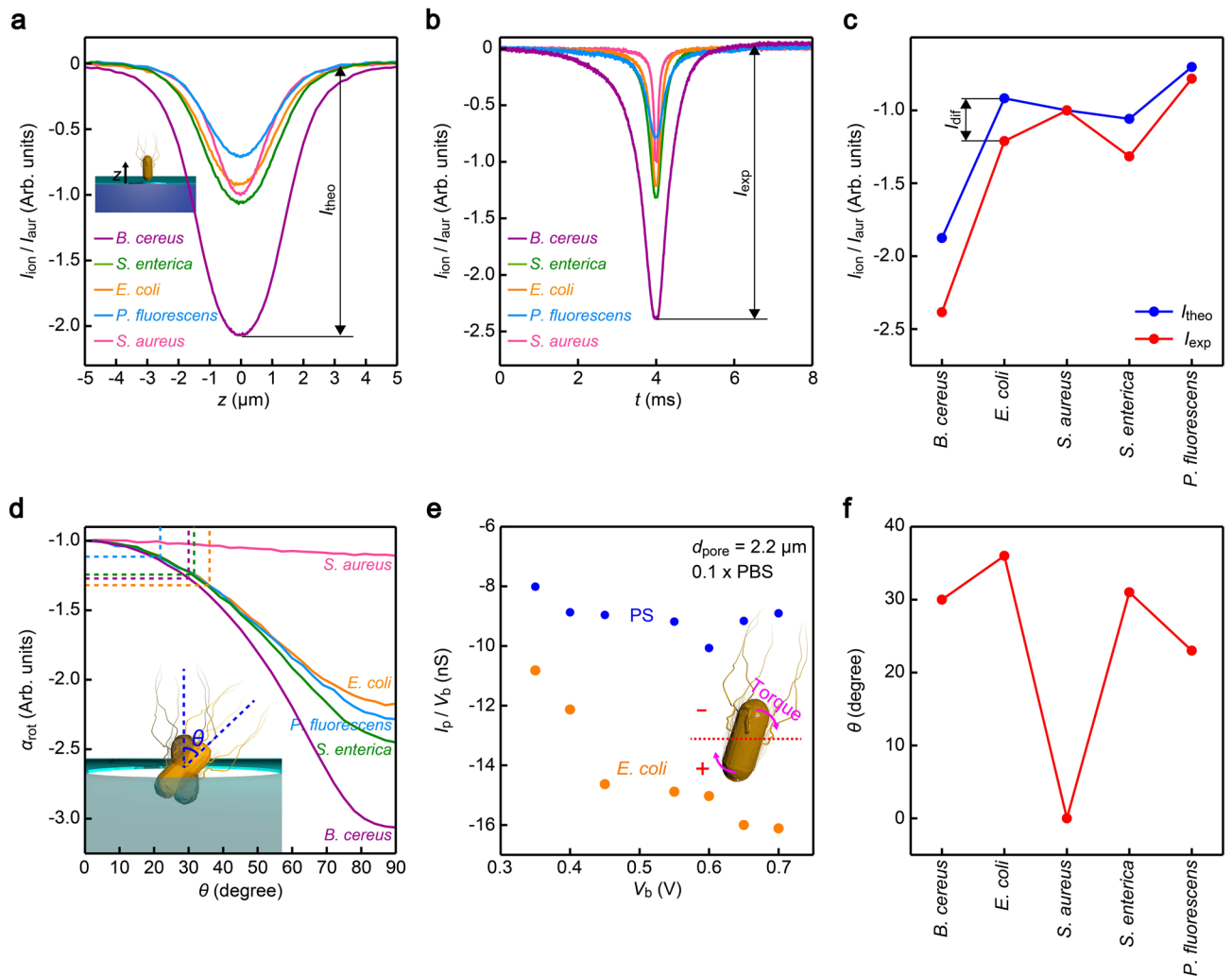


Figure 3. Bacterial orientation dependent resistive pulse waveforms. **(a)** Resistive pulses of the five bacteria simulated by a finite element analysis using COMSOL with a rod-shaped cell body moved through the 3 μm -sized pore in the 50 nm-thick SiN_x membrane along the axial direction. z scales the position of the center of mass of each bacterium from the middle of the channel as shown in the inset. Open pore current is offset to zero. The ionic current is normalized by the pulse height of *S. aureus* [I_{aur}]. I_{theo} denotes the height of each pulse. **(b)** Average resistive pulses calculated from more than 800 resistive pulses obtained for each bacterium. The longitudinal axis is normalized by I_{aur} . The heights of the pulses are described by I_{exp} . **(c)** Plots of I_{theo} and I_{exp} for the five bacteria. I_{dif} represents the deviations between the simulation and the experimental data. **(d)** Theoretically-estimated change in the resistive pulse height by the rotation of the bacteria in the center of the micropore at the angle θ . α_{rot} represents the amount of increase in the heights with respect to those at $\theta=0$. Dashed lines point to α_{rot} deduced from (c) under an assumption of $\alpha_{\text{rot}} = I_{\text{dif}}$. **(e)** Voltage dependence of the resistive pulse heights of 1.1 μm -sized carboxylated polystyrene (PS) particles (blue) and *E. coli* (orange). Inset image explains a possible torque exerted on the bacteria upon moving through the micropore via the involved galvanotactic response against the electric stimuli. **(f)** θ back-calculated from α_{rot} .

signals recorded in the experiments (Fig. 3b, see also Fig. S1). Here, we normalized the ionic current by the signal height for the quasi-spherical *S. aureus* I_{aur} . The results revealed underestimations of the resistive pulse heights in the finite element analysis for the non-spherical microbes (Fig. 3c). This can be ascribed to tilted bacterial conformations during the actual translocation in the experiments that differ from the vertical configurations assumed in the simulations. Indeed, the model calculations revealed a non-linear increase in the pulse height with the bacterial tilting angle θ for all of the five species (Fig. 3d), whose effect is also found to be dependent on the microbial aspect-ratio motifs demonstrating a factor (α_{rot}) of 1.1 for the quasi-spherical *S. aureus* while larger than 2 in cases of the other rod-shaped bacteria.

In this regard, it is noticeable that bacterial motility known as galvanotaxis would induce tilting motions under the focused in-pore electric field, wherein beating kinetics of cilia generates torque to rotate the rod-like cell body in response to the electrical stimuli^{25,26}. To verify its possible role on the translocation dynamics, we extended the resistive pulse measurements to different V_b conditions (Fig. 3e, see also Figs. S2-S3). A control test (Fig. S4) on 1.1 μm -sized carboxylated polystyrene microbeads showed almost constant $G_p = I_p/V_b$ suggesting linear increase in the ionic current with the applied voltage following the ohm's law. In sharp contrast, *E.*

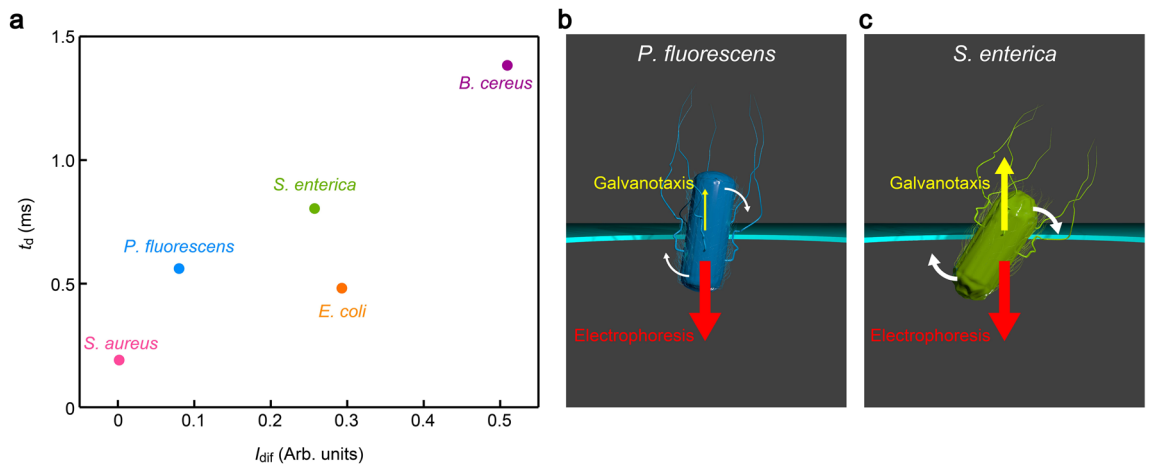


Figure 4. Galvanotaxis-derived retarded bacterial translocation. **(a)** Plots of the resistive pulse width t_d as a function of I_{dif} . **(b, c)** *P. fluorescens* showing relatively small I_{dif} is predicted to exhibit weak galvanotactic response that leads to shorter t_d **(b)**, while the translocation speed of *S. enterica* with larger I_{dif} is lowered more significantly by the field-induced bacterial motility **(c)**.

coli yielded a steady increase in G_p with V_b . The result implies a higher chance of having more tilted rod-shaped body in the pore under the larger electric field via the galvanotaxis-derived faster rotation motions (Fig. 3e).

Taking the electric field-derived ciliary motions of microbes into account, we deduced their most-likely tilting angle in the micropore. When assuming that I_{dif} stems solely from the varying orientations of the cell bodies (Fig. 3c), the ratio I_{exp}/I_{theo} can be regarded as equal to the deviation α_{rot} (Fig. 3e). From this, we roughly estimated θ that indicated prominent roles of the unique motility to render bacteria-specific conformations with *E. coli* being the most oblique one (Fig. 3f).

Besides the rotation, the galvanotactic response is known to add a momentum to move the negatively-charged bacterium in direction opposite to the electrophoresis^{25,26}. Indeed, plots of the resistive pulse width t_d against I_{dif} elucidated longer translocation time for the microbes exhibiting larger contributions of galvanotaxis (Fig. 4a), which can be interpreted as a consequence of the slower electrophoretic speed under the stronger back-force (Fig. 4b,c). *E. coli* is an exception displaying relatively short t_d that would be due to the shorter effective distance the large- θ bacterium travels within t_d . The overall findings consistently indicated the prominent role of galvanotaxis on the I_{ion} signal profiles.

We now quantify the discriminability of the five bacteria by the resistive pulse shapes. Usually, the single-cell analysis is implemented by looking at the signal heights^{10,27} that allows statistical discriminations of bacterial species as far as there is clear difference in the cell size^{28–31}. On the other hand, the above results elucidated the peculiar sensitivity of the ionic current blockage in the low-aspect-ratio micropores on non-volume properties including the bacterial shape and motility. This calls for an analytical method that enables to leverage not only the pulse height but also finer features for distinguishing the ionic current signals. Therefore, we herein employed a classifier ensemble approach of Rotation Forest³² in WEKA³³ to interrogate the resistive pulse patterns in a high-dimensional feature space. Specifically, we meshed the I_{ion} —time domain into $d_h \times d_w$ regions (Fig. 5a) and counted the number of plots in each section (Fig. 5b). We also extracted researcher-crafted parameters from the signals such as the pulse height I_p , width t_d , bluntness β , onset angle θ_{on} , area A , pulse asymmetry r_m , and inertia I_{lat} and I_{ver} , as summarized in Fig. S5. All of these were randomly selected to create 60 feature vectors and utilized for training 67 Rotation Forest ensembles (Fig. 5c,d). The algorithm then carried out the first classification for the resistive pulse data sets of known bacteria. Afterward, it internally exhibited a principal component analysis to choose the effective parameters with respect to the pretest scores, *i.e.* the number of correct outputs for judging labelled input signals, and subsequently used them to newly generate feature vectors for the post single-pulse discriminations (Fig. 5e). In this way, one can simultaneously use the multiple features on the same footing for classifying the varying pulse patterns reflecting the stochastic translocation motions of the motile bacteria.

The actual analysis was exhibited for randomly-chosen 87 resistive pulses. Among the signals, 79 were used for training classifiers to testify the discriminability of the bacteria by actually implementing resistive pulse classification for the rest of 8 pulses (tenfold cross validation). From the output of the algorithm on each labelled signals, we estimated the rate of true-negative, true-positive, false-negative, and false-positive cases. The result is summarized in a form of confusion matrix (Fig. 5f) that illustrates the high discriminability of the five bacteria with F -measure score F_{meas} reaching 0.91, which suggests 91% accuracy for identifying the bacteria from the I_{ion} signature profiles at a single-cell level. This discriminability can be judged as good considering the worst case be $F_{meas} = 0.2$ by a random guess of the five species.

It is of interest to know what enabled the single-bacteria discriminations. Nonetheless, it is not possible to figure out which of the researcher-defined parameters played an important role on the classifications due to the non-physical meaning of the internally-created feature vectors in the ensemble learning algorithm. Yet, we could at least confirm that the results were not affected by factors other than physical features of the bacterial cells. For instance, the bacterial concentration in the suspension was found to cause no notable influence on the signal waveforms (Fig. S6). This is ascribed to the principle of the ionic current blockage that reflects only the physical

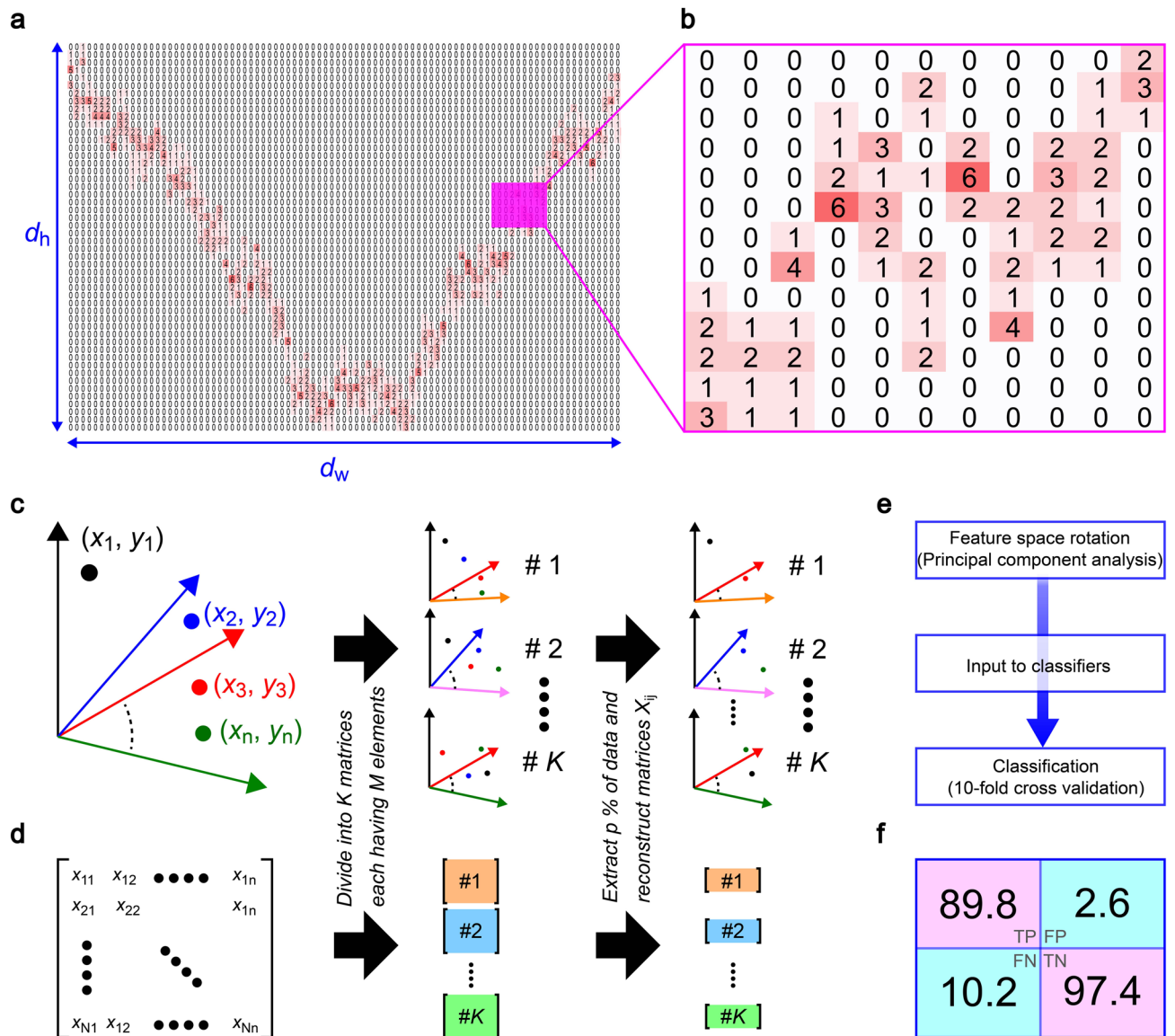


Figure 5. Machine learning-driven resistive pulse analyses. (a) Main feature parameters defined in the two-dimensional map of a resistive pulse in the $I_{ion} - t$ domain. (b) The number of data points in each mesh of the $d_h \times d_w$ sections is used as feature parameters. (c, d) Schematic (c) and mathematic (d) explanations of the ensemble learning approach for classifying the resistive pulses in a high-dimensional feature space. (e) The algorithm includes a principal component analysis to select the effective features and redefine a new set of vectors accordingly for the classification. (f) Confusion matrix showing a high precision better than 89% to identify single-bacteria among the 5 different species. TP, TN, FP, and FN denote true positive, true negative, false positive, and false negative, respectively.

properties of objects passing through the sensing zone. Moreover, dead cells were observed to be not able to transit the pore (Fig. S7), and hence they were not detected, due presumably to the denatured surface proteins with less charges that render inadequate electrophoretic forces to draw the cells captured into the channel. In fact, the present study used fresh bacterial samples by cultivating on the day of the resistive pulse measurements to minimize the population of dead cells. Although this does not rule out the possible translocation of cell fragments during the experiments, their small sizes are naturally anticipated to cause ionic current drops that are too small to be detected under the given noise floor (Fig. S8).

While the training process is laborious and time-consuming due in part to the involved pulse extractions from the $I_{ion} - t$ data recorded at the 1 MHz sampling rate, the actual single-pulse classification per se requires less than a millisecond with a standard CPU. The machine-learning-driven resistive pulse analysis can therefore be a real-time method for label-free identifications of single-bacteria. The sensor concept is also viable to virtually any bacteria as long as they can be put through the sensing zone, the capability of which may find various bioanalytical applications let alone the case sensitive pretreatments required to ensure no inclusion of oversized objects in samples that may potentially clog the channel.

Conclusions

Single-cell identifications of clinically important pathogenic bacteria were examined by a machine learning-driven resistive pulse analysis using a low aspect-ratio micropore. The shallow channel structure rendered a particular sensitivity of the blockade ionic current to the three-dimensional translocation motions of the microbes that enabled to find distinct signatures of their unique motility under the imposed electric field in the signal profiles. In order to compare and discern the bacteria-specific nontrivial features in the resistive pulses, we exhibited data classification based on an ensemble-learning algorithm in a high-dimensional feature space, which was proven useful to detect and identify the physically resembling five bacteria in real time at the single-cell level.

Methods

Preparation of bacteria. Following bacteria were used as model microorganisms for micropore analysis. *Staphylococcus aureus* (No. 13276, NITE Biological Resource Center, Japan), *Pseudomonas fluorescens* (isolated strain from food sample donated from Meiji Co. Ltd., Japan), *Salmonella enterica* (JCM 1652, RIKEN BioResource Center, Japan), *Escherichia coli* (No. 3972, NITE Biological Resource Center, Japan) and *Bacillus cereus* (JCM 2152, RIKEN BioResource Center, Japan). *E. coli*, *B. cereus*, *S. aureus* were cultivated aerobically in Trypticase Soy Broth (pH 7.3) containing 1.7% Bacto tryptone, 0.3% Bacto Soytone, 0.25% Glucose, 0.5% Sodium chloride, 0.25% Dipotassium hydrogen phosphate in ultrapure water. *S. enterica* and *P. fluorescens* were cultivated aerobically in Nutrient Broth (pH 7.0) containing 0.5% Bacto peptone, 0.3% Difco Beef extract and 0.5% Sodium chloride in ultrapure water. *E. coli*, *S. aureus* and *S. enterica* were cultured at 37 °C while *B. cereus* and *P. fluorescens* were cultured at 30 °C for 4 h after preculture under same conditions. After culture, cells were centrifuged at 1000 g for 10 min, washed twice and resuspended in 0.1 × PBS, phosphate buffered saline containing 0.08% sodium chloride, 0.002% potassium chloride, 0.012% sodium monohydrogen phosphate, and 0.02% potassium dihydrogen phosphate at pH 7.4.

Fabrication of low-aspect-ratio micropores. A Si wafer diced into 30 mm square chips was used as a substrate. On the both sides of the Si layers, there were 50 nm thick SiN_x formed by low-pressure chemical vapor deposition. The bottom side of the SiN_x was partially removed by reactive ion etching through a metal mask having a square window of 1 mm × 1 mm size. The exposed Si was immersed in KOH aq. and heated to 80 degrees Celsius for wet etching, which led to formation of a SiN_x membrane at the other side of the chip. On the membrane, electron beam resist was spin-coated and baked at 180 degrees Celsius. A circle of 3 μm diameter was delineated by electron beam lithography. After development, the residual resist was used as a mask to open the micropore by isotropic reactive ion etching of the exposed SiN_x.

Back-side polymer coating. On the back-side of the micropore chip, we spin-coated a polymethyl methacrylate (PMMA) layer of about 5 μm thickness. After baking, we irradiated electron beam from the front side of the surface at 50 μm around the micropore followed by development to remove the PMMA in the micropore.

Micropore sealing. Two blocks made of polydimethylsiloxane (PDMS) were used to seal the micropore. These blocks were made by curing PDMS on a Si substrate with an SU-8 layer patterned to have a straight motif of 15 mm length and 100 μm thickness. After polymerization in oven at 80 degrees Celsius, the blocks were cut out with knife. Because of the SU-8 pattern, there was a fluidic channel formed on the bottom surface of the PDMS block. In prior to the sealing, the channel side of the PDMS block as well as the micropore chip was exposed to oxygen plasma for surface activation. Subsequently, the two surfaces were attached together for eternal bonding. This process was repeated again for another PDMS block to seal the other side of the micropore.

Ionic current measurements. Through holes punched in the PDMS block, we injected PBS containing bacteria at one side of the micropore and bacteria-free buffer at the other side. Ag/AgCl rods were then placed at the both sides of the micropore. The ionic current through the micropore was measured by applying dc voltage between the Ag/AgCl and recording the output current through a custom-built preamplifier backed by a fast digitizer at a 1 MHz sampling rate.

Finite element analysis. The ionic current through the micropore was simulated by a finite element method. A three-dimensional model was constructed, which was composed of a cylindrical cell of 50 μm diameter and 100 μm height with a 50 nm thick SiN_x disk at the middle. A 3 μm-sized micropore was opened in the disk and the cell was filled with water containing Na⁺ and Cl⁻ ions at a concentration of 13.7 mM. The electric potential at one end was set to 0 V while the other side to +0.05 V. The ionic current was calculated by solving Poisson-Nernst-Planck and Navier-Stokes equations in a self-consistent manner using COMSOL Multiphysics 5.4.

Machine learning-driven resistive pulse pattern analysis. Classification of resistive pulse patterns was performed using the machine learning workbench WEKA with Rotation Forest ensembles each employing a distinct base classifier. Researcher-crafted feature parameters were defined and exploited in a machine learning-based classification of resistive pulses. These are: the height I_p ; the width t_d ; the bluntness at the pulse apex β_{apex} ; the onset angle θ , the pulse peak position r ; the area A ; the ratio r_m between the area before and after the peak maximum; the inertia I_m and I_w calculated with respect to longitudinal and transverse axes, respectively (detailed definitions of these parameters are explained in Fig. S5). The feature parameters were obtained from each resistive pulse data. Each parameter was coupled to the current vector and the time vector to create feature vectors,

which were then used for training classifiers. 90% of the 87 resistive pulses of known bacteria were used for the training, and the trained classifiers judged the other 10%. The average accuracy of the bacterial discrimination was assessed by repeating this procedure ten times through interchangeably changing the teacher data and the test data (tenfold cross validation). The F -measure score $F_{\text{meas}} = 2P_{\text{Pre}}P_{\text{Rec}}/(P_{\text{Pre}} + P_{\text{Rec}})$ was deduced as an average of the whole combinations of the classifiers and the feature vectors, where P_{Pre} and P_{Rec} are the precision and recall calculated through $\text{TP}/(\text{TP} + \text{FP})$ and $\text{TP}/(\text{TP} + \text{FN})$, respectively, with TP, FP, and FN being the number of true-positive, false-positive, false-negative cases, respectively, estimated from the output for the labelled resistive pulse data.

Data availability

All data and material are available for readers in methods and supplementary information.

Received: 31 March 2020; Accepted: 2 September 2020

Published online: 23 September 2020

References

- Chen, J., Andler, S. M., Goddard, J. M., Nugen, S. R. & Rotello, V. M. Integrating recognition elements with nanomaterials for bacteria sensing. *Chem. Soc. Rev.* **46**, 1272–1283 (2017).
- Zhang, Y., Lu, H. & Bargmann, C. I. Pathogenic bacteria induce aversive olfactory learning in *Caenorhabditis Elegans*. *Nature* **438**, 179–184 (2005).
- Baumler, A. J. & Sperandio, V. Interactions between the microbiota and pathogenic bacteria in the gut. *Nature* **535**, 85–93 (2016).
- Jones, K. E. *et al.* Global trends in emerging infectious diseases. *Nature* **451**, 990–993 (2008).
- Gu, H., Ho, P.-L., Tsang, K. W. T., Wang, L. & Xu, B. Using biofunctional magnetic nanoparticles to capture vancomycin-resistant enterococci and other gram-positive bacteria at ultralow concentration. *J. Am. Chem. Soc.* **125**, 15702–15703 (2003).
- Zaman, S. B. *et al.* A review on antibiotic resistance: Alarm bells are ringing. *Cureus* **9**, e1403 (2017).
- Donnarumma, G. *et al.* Effect of temperature on the shift of *Pseudomonas Fluorescens* from and environmental microorganism to a potential human pathogen. *Intl. J. Immun. Pharm.* **23**, 227–234 (2010).
- Bottone, E. J. *Bacillus Cereus*, a volatile human pathogen. *Clin. Microbiol. Rev.* **23**, 382–398 (2010).
- Schwarz-Linek, U. *et al.* Pathogenic bacteria attach to human fibronectin through a tandem β -zipper. *Nature* **438**, 177–181 (2003).
- Henriquez, R. R., Ito, T., Sun, L. & Crooks, R. M. The resurgence of Coulter counting for analyzing nanoscale objects. *Analyst* **129**, 478–482 (2004).
- Tsutsui, M. *et al.* Single-nanoparticle detection using a low-aspect-ratio pore. *ACS Nano* **6**, 3499–3505 (2012).
- Davenport, M. *et al.* The role of pore geometry in single nanoparticle detection. *ACS Nano* **6**, 8366–8280 (2012).
- Arjmandi-Tash, H. *et al.* Zero-depth interfacial nanopore capillaries. *Adv. Mater.* **30**, 1703602 (2018).
- Tsutsui, M. *et al.* Discriminating single-bacterial shape using low-aspect-ratio pores. *Sci. Rep.* **7**, 17371 (2017).
- Yusko, E. C. *et al.* Real-time shape approximation and fingerprinting of single proteins using a nanopore. *Nat. Nanotechnol.* **12**, 360–367 (2017).
- Arjmandi, N., Roy, W. V., Lagae, L. & Borghs, G. Measuring the electric charge and zeta potential of nanometer-sized objects using pyramidal-shaped nanopores. *Anal. Chem.* **84**, 8490–8496 (2012).
- Robertson, J. W. F. *et al.* Single-molecule mass spectrometry in solution using a solitary nanopore. *Proc. Natl. Acad. Sci. USA* **104**, 8207–8211 (2007).
- Tsutsui, M., Yokota, K., Arima, A., He, Y. & Kawai, T. Solid-state nanopore time-of-flight mass spectrometer. *ACS Sens.* **4**, 2974–2979 (2019).
- Hou, X. & Jiang, L. Learning from nature: Building bio-inspired smart nanochannels. *ACS Nano* **3**, 3339–3342 (2009).
- Arima, A. *et al.* Identifying single viruses using biorecognition solid-state nanopores. *J. Am. Chem. Soc.* **140**, 16834–16841 (2018).
- Tsutsui, M. *et al.* Particle trajectory-dependent ionic current blockade in low-aspect-ratio pores. *ACS Nano* **10**, 803–809 (2016).
- Rosenstein, J. K., Wanunu, M., Merchant, C. A., Drndic, M. & Shepard, K. L. Integrated nanopore sensing platform with sub-microsecond temporal resolution. *Nat. Methods* **9**, 487–492 (2012).
- Tsutsui, M. *et al.* Temporal response of ionic current blockade in solid-state nanopores. *ACS Appl. Mater. Interfaces* **10**, 34751–34757 (2018).
- Hall, J. E. Access resistance of a small circular pore. *J. Gen. Physiol.* **66**, 531–532 (1975).
- Pgawa, N., Oku, H., Hashimoto, K. & Ishikawa, M. A. Physical model for galvanotaxis of *Paramecium* cell. *J. Theor. Biol.* **242**, 314–328 (2006).
- Lytle, D. A., Johnson, C. H. & Rice, E. W. A systematic comparison of the electrokinetic properties of environmentally important microorganisms in water. *Colloid. Surf. B* **24**, 91–101 (2002).
- Kubitschek, H. E. & Friske, J. A. Determination of bacterial cell volume with the Coulter counter. *J. Bacteriol.* **168**, 1466–1467 (1986).
- Leclercq-Perlat, M. N., Bergere, J. L. & Corrieu, G. Quantitative method for enumeration of yeast cells in surface of soft cheese. *Lait* **75**, 151–158 (1995).
- Allman, R., Hann, A. C., Manchee, R. & Lloyd, D. Characterization of bacteria by multiparameter flow cytometry. *J. Appl. Bacteriol.* **73**, 438–444 (1992).
- Song, Y. X. *et al.* Counting bacteria on a microfluidic chip. *Anal. Chim. Acta* **681**, 82–86 (2010).
- Yu, A. C. S., Loo, J. F. C., Yu, S., Kong, S. K. & Chan, T. F. Monitoring bacterial growth using tunable resistive pulse sensing with a pore-based technique. *Appl. Microbiol. Biotechnol.* **98**, 855–862 (2014).
- Rodrigues, J. J., Kuncheva, L. I. & Alonso, C. J. Rotation Forest: A new classifier ensemble method. *IEEE Trans. Pattern Anal. Mach. Intell.* **28**, 1619–1630 (2006).
- Frank, E., Hall, M., Trigg, L., Holmes, G. & Witten, I. H. Data mining in bioinformatics using Weka. *Bioinformatics* **20**, 2479–2481 (2004).

Acknowledgements

A part of this work was supported by ImPACT Program of Council for Science, Technology, and Innovation (Cabinet Office, Government of Japan), the Japan Society for the Promotion of Science (JSPS) KAKENHI Grant Number 19K22108 and 18H01795, and The Food Science Institute Foundation, Ryoushokukenyukai (Tokyo, Japan).

Author contributions

T.W., T.K., and M.O. planned the research. L.I.W. and M.Tsutsui fabricated micropores. S.H., R.S., M. Tsutsui, A.A., M.Tanaka, and K.Y. performed measurements and analyzed data. M.Tsutsui, T.W., T.K., and M.O. co-wrote the paper. All authors reviewed the manuscript.

Competing interests

The authors declare no competing interests.

Additional information

Supplementary information is available for this paper at <https://doi.org/10.1038/s41598-020-72508-3>.

Correspondence and requests for materials should be addressed to M.T., T.K. or M.O.

Reprints and permissions information is available at www.nature.com/reprints.

Publisher's note Springer Nature remains neutral with regard to jurisdictional claims in published maps and institutional affiliations.



Open Access This article is licensed under a Creative Commons Attribution 4.0 International License, which permits use, sharing, adaptation, distribution and reproduction in any medium or format, as long as you give appropriate credit to the original author(s) and the source, provide a link to the Creative Commons licence, and indicate if changes were made. The images or other third party material in this article are included in the article's Creative Commons licence, unless indicated otherwise in a credit line to the material. If material is not included in the article's Creative Commons licence and your intended use is not permitted by statutory regulation or exceeds the permitted use, you will need to obtain permission directly from the copyright holder. To view a copy of this licence, visit <http://creativecommons.org/licenses/by/4.0/>.

© The Author(s) 2020